The Astronomical Journal, 153:40 (11pp), 2017 January
doi:10.3847/1538-3881/153/1/40


# THE STELLAR OBLIQUITY, PLANET MASS, AND VERY LOW ALBEDO OF QATAR-2 FROM K2 PHOTOMETRY

Fei Dai[1], Joshua N. Winn[1,2], Liang Yu[1], and Simon Albrecht[3]
[1] Department of Physics and Kavli Institute for Astrophysics and Space Research, Massachusetts Institute of Technology, Cambridge, MA 02139, USA; fd284@mit.edu
[2] Department of Astrophysical Sciences, Peyton Hall, 4 Ivy Lane, Princeton, NJ 08540, USA
[3] Stellar Astrophysics Centre, Department of Physics and Astronomy, Aarhus University, Ny Munkegade 120, DK-8000 Aarhus C, Denmark
*Received 2016 September 5; revised 2016 November 14; accepted 2016 November 15; published 2017 January 3*

## ABSTRACT

The Qatar-2 transiting exoplanet system was recently observed in short-cadence mode by *Kepler* as part of *K2* Campaign 6. We identify dozens of starspot-crossing events, when the planet eclipses a relatively dark region of the stellar photosphere. The observed patterns of these events demonstrate that the planet always transits over the same range of stellar latitudes and, therefore, that the stellar obliquity is less than about 10°. We support this conclusion with two different modeling approaches: one based on explicit identification and timing of the events and the other based on fitting the light curves with a spotted-star model. We refine the transit parameters and measure the stellar rotation period ($18.5 \pm 1.9$ days), which corresponds to a "gyrochronological" age of $1.4 \pm 0.3$ Gyr. Coherent flux variations with the same period as the transits are well modeled as the combined effects of ellipsoidal light variations ($15.4 \pm 4.8$ ppm) and Doppler boosting ($14.6 \pm 5.1$ ppm). The magnitudes of these effects correspond to a planetary mass of $2.6 \pm 0.9\ M_{\rm Jup}$ and $3.9 \pm 1.5\ M_{\rm Jup}$, respectively. Both of these independent mass estimates agree with the mass determined by the spectroscopic Doppler technique ($2.487 \pm 0.086\ M_{\rm Jup}$). No occultations are detected, giving a $2\sigma$ upper limit of 0.06 on the planet's visual geometric albedo. We find no evidence for orbital decay, although we are only able to place a weak lower bound on the relevant tidal quality factor: $Q'_\star > 1.5 \times 10^4$ (95% confidence).

*Key words:* planetary systems – planets and satellites: general – stars: individual (Qatar-2)

## 1. INTRODUCTION

The obliquity of a planet-hosting star (the angle between the star's rotation axis and its orbit normal) may bear information about a planet's formation, migration, and tidal evolution history (Queloz et al. 2000; Ohta et al. 2005; Gaudi & Winn 2007; Winn et al. 2010). For example, dynamically hot scenarios for hot-Jupiter formation, such as planet–planet scattering (Chatterjee et al. 2008) and the Kozai–Lidov mechanism (Fabrycky & Tremaine 2007), should often produce large obliquities. Dynamically cold scenarios, such as disk migration (Lin et al. 1996) and in situ formation (Batygin et al. 2015), should preserve low obliquities, unless there are mechanisms for exciting obliquities independently of hot-Jupiter formation (e.g., Bate et al. 2010; Batygin 2012).

One way to determine stellar obliquity—or, to be more precise, to recognize when the obliquity is low—is to observe a sequence of flux anomalies that occur when a transiting planet repeatedly passes in front of a starspot. The analysis of these "starspot-crossing anomalies" takes advantage of the precise time-series photometry that is available for the systems that have been observed by the *Kepler* and *CoRoT* spacecraft. This method does not require intensive time-series spectroscopy, unlike the more traditional method based on the Rossiter–McLaughlin effect, which is often difficult to apply to relatively faint or slowly rotating stars.

Silva (2003) anticipated the observable signal of a transiting planet crossing over a starspot: loss of light is temporarily reduced, because the starspot has a lower intensity than the surrounding photosphere. This produces a brief flux enhancement or "bump" in the transit light curve. It soon became clear that spot-crossing anomalies can be used to study the properties of starspots (Silva-Valio et al. 2010), demonstrate the presence of active latitudes (Sanchis-Ojeda & Winn 2011), and constrain the stellar obliquity (Nutzman et al. 2011; Sanchis-Ojeda et al. 2011).

Qatar-2b is a hot Jupiter with a mass of 2.5 $M_{\rm Jup}$, a radius of 1.1 $R_{\rm Jup}$, and an orbital period of 1.34 days. It was discovered by the Qatar Exoplanet Survey (Bryan et al. 2012). The host star Qatar-2A is a relatively bright K-dwarf ($V = 13.3$, $M_\star = 0.740 \pm 0.037\ M_\odot$). Radial-velocity follow-up revealed the presence of a long-term trend, which was attributed to a more distant companion. Mancini et al. (2014) constrained the obliquity of Qatar-2b using spot-crossing anomalies seen in ground-based multi-color transit observations. However, the stellar rotation period was unknown at the time of their analysis. Without the ability to calculate the rotational phase of each transit, Mancini et al. (2014) had to make the assumption that two particular spot-crossing anomalies they observed were caused by eclipses of the same spot. With this assumption, they found the stellar rotation period to be $14.8 \pm 0.3$ days (after the correction described by Mancini et al. 2016) and the sky-projected obliquity (the angle between the sky projections of the stellar rotation axis and the orbit normal) to be $\lambda = 4.^\circ3 \pm 4.^\circ5$.

Qatar-2 was within the field of view of *K2* Campaign 6. Being a confirmed planet, Qatar-2 was selected for 1 minute ("short-cadence") time sampling, instead of the usual 30 minute sampling. The precise, continuous, and well-sampled *K2* photometric data provide an opportunity to study Qatar-2b in greater detail. As we will show, the *K2* data reveal the stellar rotation period to be $18.5 \pm 1.9$ days, at odds with the period determined by Mancini et al. (2014). Moreover, the *K2* data show evidence for numerous spot-crossing anomalies caused by different spot groups. This leaves little room for doubt in the

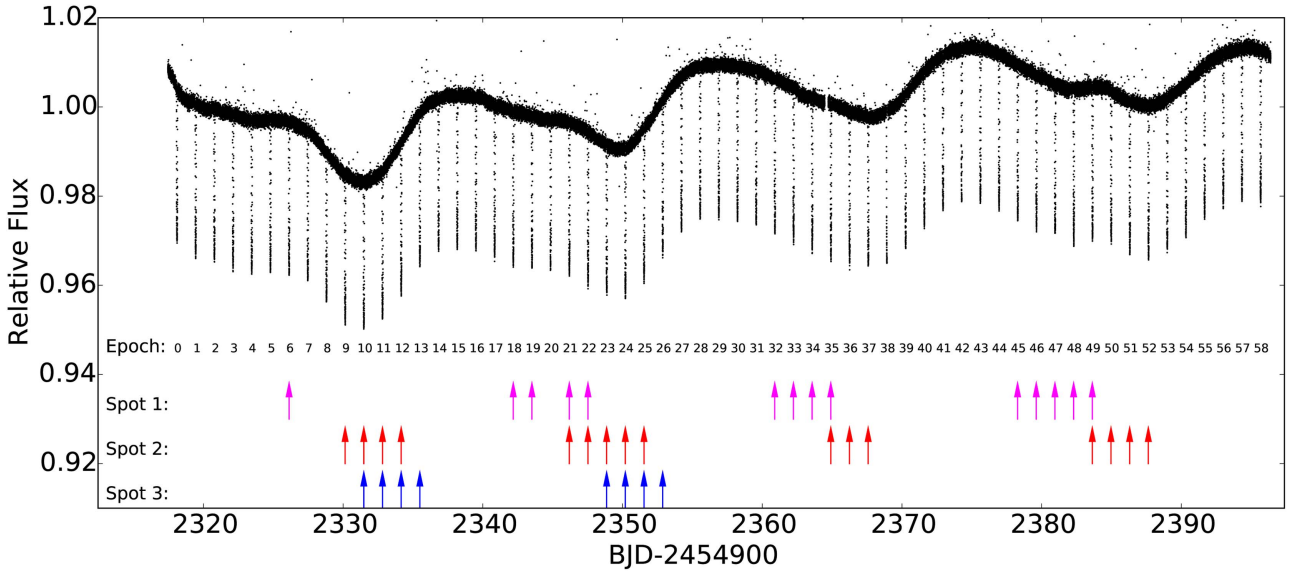


**Figure 1.** Corrected *K2* photometry of Qatar-2. Colored arrows indicate the times of identified spot-crossing anomalies (see Table 3 for the full list of anomalies and Section 7.1 for how the anomalies were grouped). Anomalies recur in groups of ≈4, on a timescale similar to the stellar rotation period of ≈18 days.

interpretation of these events and the conclusion that the stellar obliquity is low. The short-cadence data also allow for better resolution of the ingress/egress phases of the transit, leading to improved estimates of the basic transit parameters. The data can also be searched for occultations, which would reveal the planet's dayside brightness, and for ellipsoidal light variations (ELVs) and the effects of Doppler boosting (DB), the amplitudes of which can be used to make independent estimates of the planetary mass. Finally, the continuous sequence of transit times permits a search for any variations in the intervals between transits, which could be caused by additional orbiting bodies or tidal effects.

The paper is organized in the following way. Section 2 describes our reduction of the *K2* data. Section 3 lays out the analysis of the light curve and the refinement of transit parameters. Section 4 presents a search for changes in the transit period. Section 5 discusses the measurement of the stellar rotation period and the associated "gyrochronological" age. Section 6 presents the search for occultations, ELVs, and DB effects. Section 7 presents the analysis of spot-crossing anomalies and the implications for the stellar obliquity. Finally, Section 8 summarizes and discusses all our findings.

While this work was in the final stages of preparation, we became aware of the work of Močnik et al. (2016), who had performed a similar analysis of the same data. Our study and their study have reached similar conclusions regarding the stellar obliquity, stellar rotation period, transit-timing results, and flux modulation outside of transits. Some small differences exist in the quantitative results, which we describe in the appropriate sections.

## 2. K2 PHOTOMETRY

Qatar-2 (or EPIC 212756297) was observed during *K2* Campaign 6 from 2015 July 11 to October 3 in the short-cadence mode. We downloaded the pixel files from the Mikulski Archive for Space Telescopes website. As is now well known, the photometric precision of *K2* data is not as good as that of the original *Kepler* mission, due to uncontrolled rolling motion around the telescope's boresight combined with inter-pixel and intra-pixel sensitivity variations (Howell et al. 2014). To produce a photometric time series from the pixel-level data, we used an approach similar to that described by Vanderburg & Johnson (2014). In short, we used a circular aperture 4.5 pixels in radius centered around the brightest pixel. To determine the flux-weighted center of light, we fitted a two-dimensional Gaussian function to the flux distribution of the pixels within this aperture. We then fitted a piecewise linear function between the aperture-summed flux and the coordinates of the center of light and used the parameters of the best-fitting function to correct the aperture-summed flux time series. Figure 1 shows the corrected time series.

## 3. REFINING TRANSIT PARAMETERS

The high precision and high temporal sampling rate provided by *K2* short-cadence observations are ideal for resolving the ingress and egress phases of the transit as well as for revealing any anomalies in the transit profile. Before searching for anomalies, we used the short-cadence light curve to refine the basic transit parameters of Qatar-2b. Because the extant radial-velocity data are consistent with a circular orbit (Bryan et al. 2012), we assumed the orbit to be a circular orbit in all our analyses.[4]

We started with the corrected *K2* light curve (Figure 1) and published transit parameters (Bryan et al. 2012). We first analyzed each transit individually by isolating a 7 hr window around the expected midtransit times. To remove long-term stellar variability, we allowed the flux baseline to be a quadratic function of time, in addition to modeling loss of light due to the planetary transits. For the transit model, we used the `Python` package `Batman` by Kreidberg (2015). We adopted a quadratic limb-darkening profile. We chose not to impose any priors on the two limb-darkening coefficients because the short-cadence data proved to provide adequate constraints on both coefficients (see Table 1).

[4] The orbital eccentricity can also be constrained from the timing of the secondary eclipse; however, we did not detect the signal of the secondary eclipse in the *K2* data (see Section 6).

**Table 1**
System Parameters of Qatar-2A

| Parameter | | Ref. |
|---|---|---|
| Stellar Parameters | | |
| $T_{\rm eff}$ (K) | 4645 ± 50 | A |
| log $g$ (dex) | 4.601 ± 0.018 | A |
| [Fe/H] (dex) | −0.02 ± 0.08 | B |
| $v \sin i_\star$ (km s $^{-1}$) | 2.8 ± 0.5 | A |
| $M_\star$ ($M_\odot$) | 0.74 ± 0.037 | A |
| $R_\star$ ($R_\odot$) | 0.713 ± 0.018 | A |
| Apparent $V$ mag | 13.3 | A |
| $P_{\rm rot}$ (days) | 18.5 ± 1.9 | C |
| Age (Gyrochronology, Gyr) | 1.4 ± 0.3 | C |
| Age (Isochrone, Gyr) | 15.72 ± 1.36 | B |
| $u_1$ | 0.6231 ± 0.0057 | C |
| $u_2$ | 0.062 ± 0.015 | C |
| Planetary Parameters | | |
| $P$ (days) | 1.337116553 ± 0.000000044 | C |
| $T_c$ (BJD) | 2455617.581506 ± 0.000054 | C |
| $R_\star/a$ | 0.15350 ± 0.00018 | C |
| $a$ (au) | 0.02160 ± 0.00057 | C |
| $R_{\rm p}/R_*$ | 0.16208 ± 0.00018 | C |
| $R_{\rm p}$ ( $R_{\rm Jup}$) | 1.150 ± 0.030 | C |
| $i$ (°) | 89.7 ± 0.5 | C |
| $b$ | 0.03 ± 0.06 | C |
| $M_{p,\rm RV}$ ($M_{\rm Jup}$) | 2.487 ± 0.086 | A |
| $M_{p,\rm ELV}$ ($M_{\rm Jup}$) | 2.6 ± 0.9 | C |
| $M_{p,\rm DB}$ ($M_{\rm Jup}$) | 3.9 ± 1.5 | C |
| $e$ (assumed) | 0 | A |

**Note.** A: Bryan et al. (2012); B: Maxted et al. (2015); C: this work.

Another effect that alters the transit profile is the presence of starspots outside of the transit chord. Transit models such as `Batman` assume the photosphere to be unspotted. When spots are present, the untransited portion of the photosphere makes a smaller relative contribution to the total flux than is assumed in the model. If this is not accounted for, the model parameters would compensate for the relatively large loss of light by increasing the planet size, giving a biased result. To account for this effect, we introduced an additional parameter specific to each transit: $\Delta F_{\rm spot}$, the relative loss of light due to any unocculted spots on the visible hemisphere. The calculated flux that is compared to the observed flux is

$$F_{\rm calc,spot} = \frac{F_{\rm calc,no-spot} - \Delta F_{\rm spot}}{1 - \Delta F_{\rm spot}} \quad (1)$$

where $F_{\rm calc,spot}$ and $F_{\rm calc,no-spot}$ are the theoretical flux when unocculted starspots are taken and not taken into account, respectively. In this equation, the role of the denominator is to ensure that $F_{\rm calc,spot} \equiv 1$ outside of the transits, since the data have been normalized in this manner.

In summary, the set of parameters describing each transit comprises the time of inferior conjunction ($T_c$), the three parameters of the quadratic function of time representing stellar variability ($a_2$, $a_1$, and $a_0$), and the loss of light due to unocculted spots on the visible hemisphere ($\Delta F_{\rm spot}$). There are also the usual transit parameters: the planet-to-star radius ratio ($R_{\rm p}/R_\star$), the ratio of the stellar radius to the orbital distance ($R_\star/a$), the impact parameter ($b$), and the limb-darkening coefficients ($u_1$ and $u_2$). We adopted the usual $\chi^2$ likelihood function and found the maximum-likelihood solution using the Levenberg–Marquardt algorithm as implemented in the `Python` package `lmfit` (Newville et al. 2014).

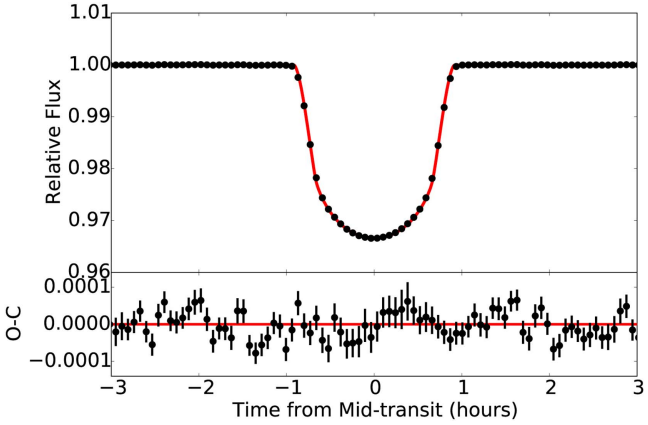


**Figure 2.** Top. Phase-folded transit light curve of Qatar-2 after being corrected for stellar variability, unocculted spots, and spot-crossing anomalies. The red line shows the best-fitting model. The data have been averaged in phase within intervals of 3 minutes. Bottom. Residuals between the data and the best-fitting model.

Spot-crossing anomalies are clearly visible in the time series of residual fluxes. These anomalies would have been a source of bias in the model parameters if no corrections had been performed. We identified these anomalies through visual inspection and modeled them as Gaussian functions of time:

$$F_{\rm anom}(t) = A \exp\left[-\frac{(t - t_{\rm anom})^2}{2\sigma_{\rm anom}^2}\right] \quad (2)$$

where $A$, $t_{\rm anom}$, and $\sigma_{\rm anom}$ represent (respectively) the amplitude, time, and duration of the anomaly.

In some cases, visual inspection of a given transit revealed more than one spot-crossing anomaly. To decide on the number of spot-crossing anomalies to include in the final model, we fitted the light curve with increasing numbers of spots and calculated the change in the Bayesian information criterion as follows:

$$\mathrm{BIC} = 2\log(L_{\rm max}) + N\log(M), \quad (3)$$

where $L_{\rm max}$ is the maximum likelihood, $N$ is the number of model parameters, and $M$ is the number of data points. We only retained those anomalies for which $\Delta\mathrm{BIC} > 10$. Table 3 reports the properties of all these anomalies. Parameter uncertainties were determined via the Markov chain Monte Carlo (MCMC) method as implemented in the `Python` package `emcee` (Foreman-Mackey et al. 2013). Here and elsewhere in this paper, the reported parameter value is based on the 50% level of the cumulative posterior distribution, and the uncertainty interval is based on the 16% and 84% levels.

We used the best-fitting parameters to correct the data from each transit for stellar variability and unocculted spots. We also removed spot-crossing anomalies by excluding data points within $2\sigma_{\rm anom}$ of the time of each anomaly. We combined all 59 of the rectified and spot-cleaned transit intervals to create a phase-folded transit light curve with a very high signal-to-noise ratio. Then we modeled this phase-folded light curve to determine the basic transit parameters, using another MCMC analysis (see Figure 2).

We then assumed that these basic transit parameters are fixed in time and applicable to each and every transit. We repeated the analysis of all of the individual transits, holding the transit parameters fixed at the values determined from the analysis of the phase-folded light curve. This in turn allowed the creation of a new version of the phase-folded light curve. After two such iterations it was clear that the results had already converged. Table 1 gives the results.

## 4. LACK OF TRANSIT-TIMING VARIATIONS

To search for evidence of any changes in the orbital period since the time of discovery of Qatar-2b, we combined our measured midtransit times with those found on the Exoplanet Transit Database website. Table 2 gives all the midtransit times in the Barycentric Dynamical Time system (Eastman et al. 2010; $\mathrm{BJD_{TBD}}$).

Figure 3 shows the residuals between the observed times and the calculated times according to the best-fitting constant-period model. The only obvious pattern in the residuals is that the data points from the second season are generally above the baseline, while the third season's data are below the baseline. It will be interesting to see if these long-term variations are seen in future seasons. We do not find any sinusoidal-like variations that are sometimes seen in multi-planet systems. We computed the Lomb–Scargle periodogram (Lomb 1976; Scargle 1982) of the timing residuals; no signal was detected with a false alarm probability less than 10%. We also did not detect any evidence for a secular change in the orbital period, as described below. The lack of detectable period shrinkage allows us to place a constraint on the rate of tidal dissipation in the system. Tidal evolution is expected to cause period decay with a rate that scales as $(M_{\rm p}/M_\star)(R_\star/a)^5$ (Levrard et al. 2009), which is relatively large for this system because of the close-in orbit. For quantitative constraints on the rate, we fitted the following function to the sequence $T_n$ of midtransit times:

$$T_n = T_0 + nP_0 + \frac{1}{2}n^2\frac{dP}{dn}. \quad (4)$$

We conducted an MCMC analysis using `emcee` and the usual $\chi^2$ likelihood function, and uniform priors for all parameters. The result for the period-change parameter was an upper limit, $\left|\frac{dP}{dN}\right| < 0.11$ milliseconds, or $\left|\frac{dP}{dt}\right| < 1.7 \times 10^{-9}$ (95% conf.). To translate these upper bounds into a lower bound on the stellar tidal quality factor, we used the following formula (Levrard et al. 2009):

$$Q'_\star = 9P^2\left(\frac{dP}{dN}\right)^{-1}\frac{M_p}{M_\star}\left(\frac{R_\star}{a}\right)^5\left(\omega_\star - \frac{2\pi}{P}\right), \quad (5)$$

where $\omega_\star$ is the angular velocity of stellar rotation. The derivation of this formula assumes a circular orbit and zero obliquity. For Qatar-2, the low eccentricity is compatible with the available radial-velocity data set (Bryan et al. 2012), and a low obliquity is implied by our analysis in Section 7. The result of applying this formula to our data is $Q'_\star > 1.5 \times 10^4$ (95% conf.).

## 5. STELLAR ROTATION PERIOD AND GYROCHRONOLOGY

The *K2* light curve (Figure 1) exhibits quasiperiodic flux variations with four cycles. These variations are characteristic

**Table 2**
Midtransit Times of Qatar-2b

| Epoch | $T_c$ (BJD—2454900) | Unc. | Ref. |
|---|---|---|---|
| −1197 | 717.58156 | 0.00082 | 1 |
| −1192 | 724.26679 | 0.00011 | 2 |
| −1141 | 792.46109 | 0.00270 | 1 |
| −1135 | 800.47915 | 0.00083 | 1 |
| −930 | 1074.59334 | 0.00072 | 3 |
| −927 | 1078.6048 | 0.0012 | 4 |
| −921 | 1086.62711 | 0.00069 | 5 |
| −894 | 1122.72850 | 0.00018 | 6 |
| −894 | 1122.72800 | 0.00017 | 7 |
| −894 | 1122.72815 | 0.00016 | 8 |
| −894 | 1122.72810 | 0.00022 | 9 |
| −891 | 1126.73842 | 0.00033 | 10 |
| −888 | 1130.7516 | 0.0015 | 11 |
| −885 | 1134.76157 | 0.00010 | 6 |
| −885 | 1134.76196 | 0.00012 | 7 |
| −885 | 1134.76198 | 0.00015 | 8 |
| −885 | 1134.76249 | 0.00015 | 9 |
| −883 | 1137.43785 | 0.00068 | 12 |
| −882 | 1138.77329 | 0.00010 | 7 |
| −882 | 1138.77345 | 0.00012 | 8 |
| −882 | 1138.77312 | 0.00015 | 9 |
| −877 | 1145.45890 | 0.00042 | 13 |
| −868 | 1157.49242 | 0.00018 | 14 |
| −868 | 1157.49246 | 0.00028 | 15 |
| −868 | 1157.49274 | 0.00016 | 16 |
| −868 | 1157.49282 | 0.00023 | 17 |
| −659 | 1436.94926 | 0.00059 | 18 |
| −657 | 1439.62434 | 0.00027 | 19 |
| −654 | 1443.6346 | 0.0011 | 20 |
| −616 | 1494.44559 | 0.00056 | 21 |
| −604 | 1510.4905 | 0.0010 | 22 |
| −603 | 1511.8302 | 0.00058 | 23 |
| −597 | 1519.8502 | 0.0013 | 24 |
| −580 | 1542.58191 | 0.00014 | 25 |
| 0 | 2318.109992 | 0.000049 | 26 |
| 1 | 2319.447169 | 0.000049 | 26 |
| 2 | 2320.784315 | 0.000050 | 26 |
| 3 | 2322.121328 | 0.000049 | 26 |
| 4 | 2323.458458 | 0.000051 | 26 |
| 5 | 2324.795643 | 0.000049 | 26 |
| 6 | 2326.132714 | 0.000090 | 26 |
| 7 | 2327.469972 | 0.000050 | 26 |
| 8 | 2328.807039 | 0.000057 | 26 |
| 9 | 2330.143911 | 0.000099 | 26 |
| 10 | 2331.481166 | 0.000050 | 26 |
| 11 | 2332.818338 | 0.000052 | 26 |
| 12 | 2334.155345 | 0.000059 | 26 |
| 13 | 2335.492644 | 0.000079 | 26 |
| 14 | 2336.829644 | 0.000096 | 26 |
| 15 | 2338.166710 | 0.000060 | 26 |
| 16 | 2339.503878 | 0.000056 | 26 |
| 17 | 2340.840863 | 0.000056 | 26 |
| 18 | 2342.177965 | 0.000071 | 26 |
| 19 | 2343.515114 | 0.000049 | 26 |
| 20 | 2344.852294 | 0.000055 | 26 |
| 21 | 2346.189436 | 0.000068 | 26 |
| 22 | 2347.526675 | 0.000090 | 26 |
| 23 | 2348.863781 | 0.000075 | 26 |
| 24 | 2350.200849 | 0.000049 | 26 |
| 25 | 2351.537860 | 0.000052 | 26 |
| 26 | 2352.875083 | 0.000068 | 26 |
| 27 | 2354.212212 | 0.000052 | 26 |
| 28 | 2355.549382 | 0.000053 | 26 |
| 29 | 2356.886369 | 0.000052 | 26 |

**Table 2**
(Continued)

| Epoch | $T_c$ (BJD—2454900) | Unc. | Ref. |
|---|---|---|---|
| 30 | 2358.223494 | 0.000054 | 26 |
| 31 | 2359.560744 | 0.000049 | 26 |
| 32 | 2360.897787 | 0.000059 | 26 |
| 33 | 2362.234890 | 0.000054 | 26 |
| 34 | 2363.572009 | 0.000055 | 26 |
| 35 | 2364.909290 | 0.000106 | 26 |
| 36 | 2366.246114 | 0.000051 | 26 |
| 37 | 2367.583411 | 0.000049 | 26 |
| 38 | 2368.920242 | 0.000078 | 26 |
| 39 | 2370.257464 | 0.000054 | 26 |
| 40 | 2371.594669 | 0.000056 | 26 |
| 41 | 2372.931863 | 0.000048 | 26 |
| 42 | 2374.269011 | 0.000055 | 26 |
| 43 | 2375.605990 | 0.000056 | 26 |
| 44 | 2376.943205 | 0.000051 | 26 |
| 45 | 2378.280327 | 0.000069 | 26 |
| 46 | 2379.617357 | 0.000051 | 26 |
| 47 | 2380.954439 | 0.000054 | 26 |
| 48 | 2382.291665 | 0.000071 | 26 |
| 49 | 2383.628818 | 0.000079 | 26 |
| 50 | 2384.965898 | 0.000053 | 26 |
| 51 | 2386.302902 | 0.000052 | 26 |
| 52 | 2387.640011 | 0.000091 | 26 |
| 53 | 2388.977140 | 0.000051 | 26 |
| 54 | 2390.314349 | 0.000050 | 26 |
| 55 | 2391.651335 | 0.000051 | 26 |
| 56 | 2392.988456 | 0.000058 | 26 |
| 57 | 2394.325632 | 0.000048 | 26 |
| 58 | 2395.662874 | 0.000052 | 26 |

**References.** (1) Canis Major Observatory (Mancini et al. 2014); (2) Bryan et al. (2012); (3) Strajnic et al. (TRESCA); (4) Zibar M. (TRESCA); (5) Gonzales J. (TRESCA); (6) MPG/ESO 2.2 m $g'$ (Mancini et al. 2014); (7) MPG/ESO 2.2 m $r'$ (Mancini et al. 2014); (8) MPG/ESO 2.2 m $i'$ (Mancini et al. 2014); (9) MPG/ESO 2.2 m $z'$ (Mancini et al. 2014); (10) Dax T. (TRESCA); (11) Masek M. (TRESCA); (12) Carreno A. (TRESCA); (13) Montigiani N., Manucci M. (TRESCA); (14) Cassini 1.52 m (Mancini et al. 2014); (15) CAHA 2.2 m $g$ (Mancini et al. 2014); (16) CAHA 2.2 m $r$ (Mancini et al. 2014); (17) CAHA 2.2 m $z$ (Mancini et al. 2014); (18) Campbell J. (TRESCA); (19) CAHA 1.23 m (Mancini et al. 2014); (20) Ren'e R. (TRESCA); (21) Ayiomamitis A. (TRESCA); (22) Jacobsen J. (TRESCA); (23) Kehusmaa P., Harlingten C. (TRESCA); (24) Shadic S. (TRESCA); (25) Colazo C., et al. (TRESCA).; (26) *K2* (this work). TRESCA stands for "Transiting Exoplanets and Candidates."

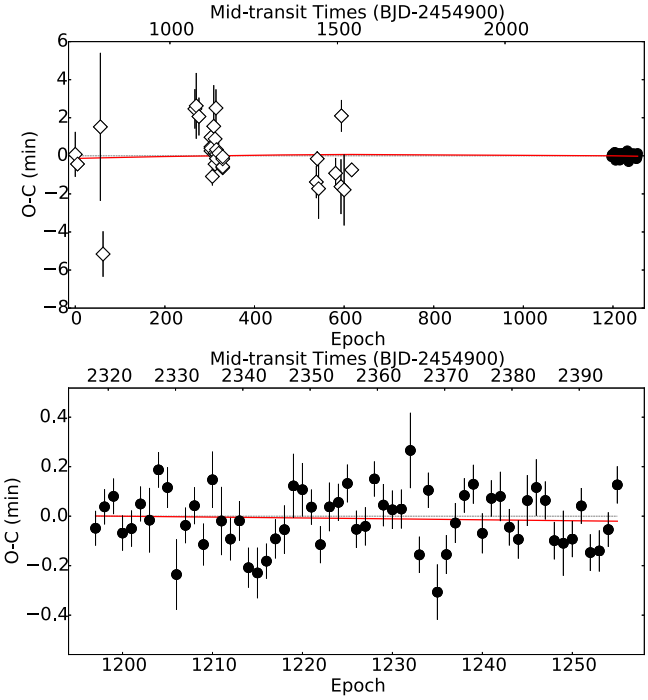


**Figure 3.** Observed minus calculated transit times of Qatar-2b, where the calculated times are based on the best-fitting constant-period model. The top panel shows all the available data, and the bottom panel allows a closer view of the *K2* data. Table 2 gives the numerical data.

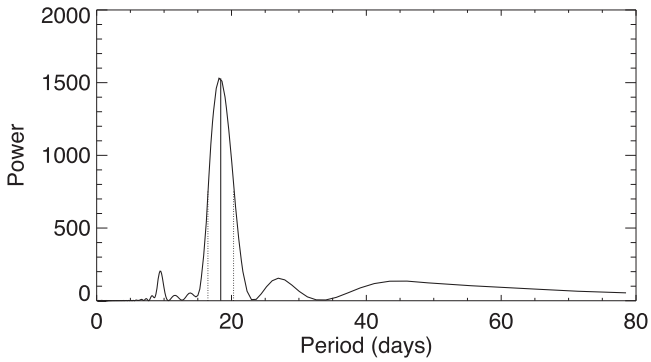


**Figure 4.** Lomb–Scargle periodogram of the out-of-transit flux variations of Qatar-2. Based on the location and width of the most prominent peak, we estimate the rotation period to be 18.5 ± 1.9 days.

of starspots being carried around by rotation, and therefore, the stellar rotation period can be estimated from the period of these flux variations. For a quantitative estimate, we masked out the transits and calculated the Lomb–Scargle periodogram (Lomb 1976; Scargle 1982) of the resulting time series, which is shown in Figure 4. Based on the location and width of the most prominent peak in the periodogram, we estimate the stellar rotation period to be 18.5 ± 1.9 days.

Knowledge of the stellar rotation period played a crucial role in our obliquity determination (see Section 7). In addition, for main-sequence stars such as Qatar-2, the rotation period is linked to the stellar age, a relationship that has come to be known as "gyrochronology." We estimated the age of the system using a gyrochronological formula that was derived by Schlaufman (2010):

$$P_\star(M_\star, \tau_\star) = P_{\star,0}(M_\star)\left(\frac{\tau_\star}{650\ \mathrm{Myr}}\right)^{1/2}, \quad (6)$$

where $P_\star(M_\star, \tau_\star)$ is the rotation period of a star with mass $M_\star$ and age $\tau_\star$ and $P_{\star,0}(M_\star)$ is a specified polynomial function that was calibrated using data from the Hyades and Praesepe star clusters. According to this formula and our measured rotation period, the gyrochronological age of Qatar-2 is 1.4 ± 0.3 Gyr.

Maxted et al. (2015) made an independent estimate of the stellar age by fitting stellar-evolutionary models to the observed spectroscopic parameters and apparent magnitudes. Their result was 15.7 ± 1.4 Gyr, significantly older than the gyro age. Assuming this older age is correct, the younger gyro age could be taken as evidence that the star has been spun up by the tidal

torque of the close-in planet. However, Maxted et al. (2015) expressed concern that their estimate is unrealistic because their method may be biased by the "inflated K-dwarf" phenomenon, a known problem with stellar-evolutionary models in fitting the observed properties of stars similar to Qatar-2.

Močnik et al. (2016) also used *K2* data to determine the stellar rotation period and found the gyro age to be $0.59 \pm 0.10$ Gyr. This is significantly younger than our estimate of the gyro age. Since their result for the rotation period was essentially equivalent to ours, the difference in gyro ages must be attributable to the different gyrochronological formula that was adopted by Močnik et al. (2016). They used a formula presented by Barnes (2007), while we used the formula above from Schlaufman (2010). Evidently, the gyro age is subject to a systematic uncertainty that is more significant than the uncertainty in the stellar rotation period.

Another use of the stellar rotation period is for estimating the inclination $i_\star$ between the stellar rotation axis and the line of sight. This is done through the following formula:

$$\sin i_\star = \frac{v \sin i_\star}{v} = \frac{v \sin i_\star}{2\pi R_\star / P_{\rm rot}}, \quad (7)$$

where $v \sin i_\star$ is the projected rotation rate that can be estimated from the degree of rotational broadening that is observed in the star's photospheric absorption lines. For Qatar-2, Bryan et al. (2012) found $v \sin i_\star = 2.8 \pm 0.5\,{\rm km\,s^{-1}}$, while our results lead to $v = 2\pi R\star / P_{\rm rot} = 2.0 \pm 0.3\,{\rm km\,s^{-1}}$, giving $\sin i_\star = 1.4 \pm 0.6$. This is compatible with unity, as expected for a low-obliquity star, although the uncertainty is large enough to encompass inclinations as low as 50° (as well as mathematically impossible values of $\sin i_\star$).

## 6. PHASE CURVE ANALYSIS AND SECONDARY ECLIPSE

Thanks to the high precision and nearly continuous temporal coverage of the *K2* data, we may perform a sensitive search for the occultation of Qatar-2b by its parent star (the secondary eclipse) as well as out-of-eclipse light variations associated with the orbital period. The latter type of variations could arise from the tidally induced ellipsoidal figure of the star (ELV), Doppler boosting (DB), and illumination effects (ILL), as exemplified by Mazeh & Faigler (2010). All of these effects are expected to be small, on the order of ~10 ppm. Thus, it is difficult—but important—to distinguish any residual systematic effects in the time series from the astrophysical effects.

For this reason, we performed all our analyses on several versions of the *K2* light curve, all of which used different algorithms to filter out systematic effects and artifacts. Specifically, we used the versions known as `K2SFF` (Vanderburg & Johnson 2014; Vanderburg et al. 2016), `K2SC` (Aigrain et al. 2016; Pope et al. 2016), `and K2 Everest` (Luger et al. 2016) and our own processed light curve. We found that while all of the light curves gave consistent results, `K2 Everest` seemed to have the lowest levels of residual systematic trends and artifacts. This particular algorithm differs from all the others as it is based on pixel-level decorrelation (Deming et al. 2015). All the other methods rely on measurements of the flux-weighted center of light of a specific collection of pixels. The results described in the rest of this section are based on the `K2 Everest` light curve.

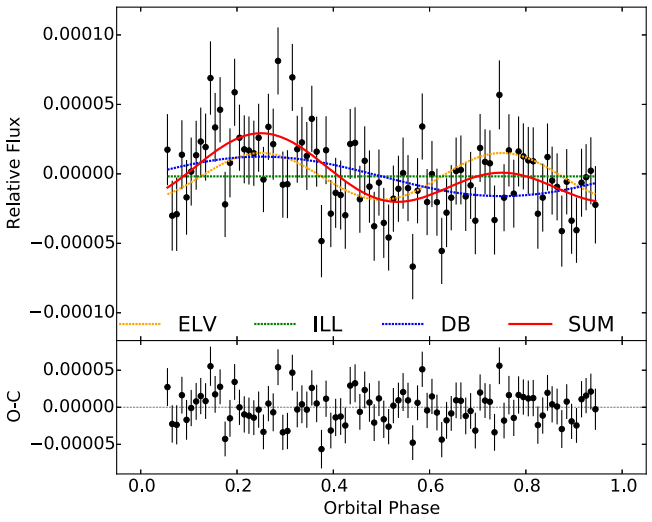


**Figure 5.** The phase-folded and binned light curve of Qatar-2 after the transits and filtering are excluded as described in the text. The red curve shows the best-fitting model. The different components of the model are shown in different colors (except the additive constant, which is not shown). No secondary eclipse was detected.

We omitted all the data within 3 hr of each midtransit time. To remove long-term stellar variability, we divided the light curve by a cubic spline with a temporal width of twice the orbital period. We then folded the time series with the orbital period of the planet and averaged the resulting light curve into 100 bins equally spaced in the orbital phase. We fitted for ELV, DB, and ILL effects simultaneously (see Figure 5). For the ILL component, we adopted a Lambertian phase function. The combined model for the variations took the form

$$F_0 - A_{\rm ELV}\cos(4\pi\phi) + A_{\rm DB}\sin(2\pi\phi) + A_{\rm ILL}\frac{\sin(z) + (\pi - z)\cos(z)}{\pi} \quad (8)$$

where

$$\cos(z) = -\sin(i)\cos(2\pi\phi + \theta) \quad (9)$$

and

$$\phi = \frac{t - T_{\rm c}}{P}. \quad (10)$$

In these equations, $F_0$ is an additive constant; $A_{\rm ELV}$, $A_{\rm DB}$, and $A_{\rm ILL}$ are the amplitudes of the ELV, DB, and ILL effects; $T_{\rm c}$ is the time of inferior conjunction; $P$ is the orbital period; $i$ is the orbital inclination; and $\theta$ represents a hypothetical offset between the maximum of the phase curve and the time of superior conjunction. We also fitted for loss of light during the secondary eclipse by using `Batman` and requiring the depth of the secondary eclipse to be consistent with $A_{\rm ILL}$. Initially, we allowed the phase of the secondary eclipse to be a free parameter; once it became clear that no secondary eclipse could be detected, we reverted to the assumption of a circular orbit and thereby required the secondary eclipse to occur at $\phi = 0.5$.

We conducted an MCMC analysis with `emcee`, with uniform priors on all the parameters. The $A_{\rm ELV}$ and $A_{\rm DB}$ parameters were both found to be nonzero. Specifically, $A_{\rm ELV} = 15.4 \pm 4.8$ ppm and $A_{\rm DB} = 14.6 \pm 5.1$ ppm. Both of these effects depend on the planet mass, along with additional system parameters that are largely constrained by

other observations. Therefore, we may use the results for $A_{\rm ELV}$ and $A_{\rm DB}$ to make independent determinations of the planet mass. For this purpose we used Equations (11), (12), and (15) of Carter et al. (2011). The mass implied by the ELV amplitude is $M_{\rm p,ELV} = 2.6 \pm 0.9\ M_{\rm Jup}$, while the mass implied by the DB amplitude is less certain, $M_{\rm p,DB} = 3.9 \pm 1.5\ M_{\rm Jup}$. These two independent estimates are consistent with each other within one sigma and also agree with the mass determination $M_{\rm p,RV} = 2.487 \pm 0.086\ M_{\rm Jup}$ based on the more secure and traditional Doppler technique (Bryan et al. 2012). This lends confidence to our assessment that the out-of-transit flux variations are astrophysical rather than being dominated by instrumental or systematic effects.

Neither an ILL effect nor a secondary eclipse was detected. The resulting upper bound on $A_{\rm ILL}$ is 35 ppm (95% conf.). This represents an upper bound on the combination of the planet's reflected light and thermal emission. Assuming that the thermal emission is negligible within the *Kepler* bandpass, the resulting upper limit on the planet's geometric albedo is $A_g < 0.06$. Any contribution from thermal emission would require an even smaller geometric albedo. Conversely, if the reflected component is assumed to be negligible, we may place an upper bound on the effective temperature of the planet, after making the simplifying assumption that the planet emits as a blackbody. The resulting upper limit is $T_{\rm eff} < 1500$ K (95% conf.). This is consistent with the calculated equilibrium temperature of $T_{\rm eq} \approx 1300$ K, assuming a Bond albedo of zero.

## 7. SPOT-CROSSING ANOMALIES AND OBLIQUITY MEASUREMENT

In this section, we present the analysis of the spot-crossing anomalies. The patterns of recurrence of the spot-crossing anomalies imply that the transit chord is aligned with the lines of latitude on the star—which in turn implies that the star has low obliquity. For quantitative analysis we employed two different approaches, each of which has its advantages and limitations.

### 7.1. Anomaly Identification and Timing

First we employed a simple geometric model for which the parameters are constrained by the measured times of spot-crossing anomalies. Similar models have previously been used to constrain the obliquity of planet-hosting stars (Nutzman et al. 2011; Sanchis-Ojeda et al. 2011). The premise is straightforward: when an anomaly is observed, the planet's position in the sky must at least partially overlap with the location of the starspot. We define our coordinate system on the plane of sky such that the $x$-axis is aligned with the line of nodes of the planetary orbit and the $y$-axis is in the perpendicular direction. Using the basic transit parameters determined earlier, we calculate the projected $x$ and $y$ coordinates of the planet as a function of time. We choose a particular spot-crossing anomaly as the nominal starting point, at which the starspot is placed at the position of the planet. Then we can predict any future or past location of the starspot given the following parameters: the stellar inclination ($i_\star$), the sky-projected obliquity ($\lambda$), the stellar rotation period ($P_{\rm rot}$), and the stellar latitude of the spot ($l$). For simplicity we assume that the starspot does not change significantly in size, intensity, or location during the interval over which the model is applied.

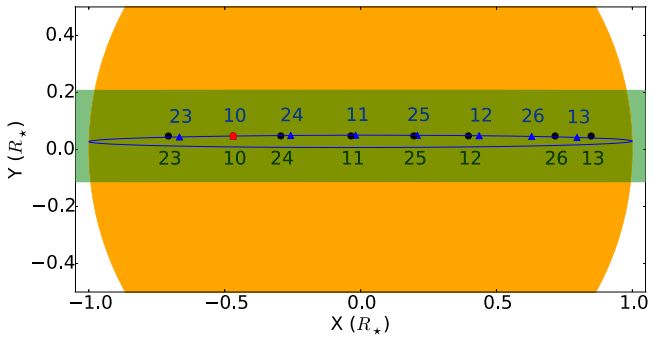


**Figure 6.** Illustration of the first modeling approach, in which we measure the times of anomalies that seem associated with a single spot, and constrain a geometric model by requiring the planet and spot to be nearly coincident on the sky plane at those times. The orange circle represents the stellar disk. The green band is the transit chord. The black circles are the calculated positions of the planet during each spot-crossing anomaly that was assigned to Spot 3 from Table 3. The numbers specify the transit epoch numbers. The blue curve is the calculated trajectory of Spot 3, and the blue triangles are the calculated locations of Spot 3 at the time of the anomalies. The success of the model is illustrated by the near-coincidence of the planet and spot at the times of all the anomalies.

This assumption is more valid on a relatively short time interval.

Figure 6 illustrates this model using the anomalies associated with Spot 3 in Table 3. The black dots show the calculated positions of the planet in each spot-crossing anomaly caused by Spot 3. We initialized the model by assuming that the spot and planet coincided at the time of the first anomaly (Epoch 10, red circle). The blue curve shows the spot's trajectory in the stellar photosphere, and the blue triangles show the calculated positions of the spot at the times of the observed anomalies. The success of the model is indicated by the close coincidence between the positions of the planet and spot.

A key question is what to do when there are multiple spots on the star, which is likely in general and is definitely the case for Qatar-2. When the model has multiple spots, how do we associate individual spot-crossing anomalies with a particular spot? First we grouped the spot-crossing anomalies into families through visual inspection of their relative phases, amplitudes, and durations. We then revised these assignments as needed when the model revealed significant outliers, indicating a mistaken association. Our final assignments are justified by the fact that all the different groups are consistent with the same rotation period, which is in turn consistent with the rotation period estimated from the *K2* light curve (see Table 4).

Although this procedure seems to work, the necessity to group the anomalies as we have just described is a shortcoming of this simple geometric model. This weakness is especially serious when the technique is applied to ground-based data, for which quasi-continuous monitoring is very difficult to achieve. For example, Mancini et al. (2014) did not have the stellar rotation period as an independent check for their model of Qatar-2b. By assuming that two particular spot-crossing anomalies they observed were associated with a single spot, they derived a stellar rotation period of $14.8 \pm 0.3$ days (as later revised by Mancini et al. 2016). This is now known to be incorrect; most likely, the two observed anomalies were produced by crossings over two different spots.

**Table 3**
Spot-crossing Anomalies Observed in K2

| Epoch | $t_{\rm anom}$ (BJD − 2454900) | Amplitude | Width (days) | No. |
|---|---|---|---|---|
| 6 | 2326.12087 ± 0.00097 | 0.00112 ± 0.00019 | 0.00503 ± 0.00123 | 1 |
| 18 | 2342.15048 ± 0.00126 | 0.00092 ± 0.00023 | 0.00416 ± 0.00086 | 1 |
| 19 | 2343.49928 ± 0.00059 | 0.00154 ± 0.00021 | 0.00336 ± 0.00049 | 1 |
| 21 | 2346.20227 ± 0.00078 | 0.00164 ± 0.00037 | 0.00597 ± 0.00158 | 1 |
| 22 | 2347.55201 ± 0.00096 | 0.00105 ± 0.00030 | 0.00307 ± 0.00099 | 1 |
| 32 | 2360.87726 ± 0.00041 | 0.00195 ± 0.00025 | 0.00296 ± 0.00048 | 1 |
| 33 | 2362.22691 ± 0.00043 | 0.00213 ± 0.00020 | 0.00387 ± 0.00043 | 1 |
| 34 | 2363.57898 ± 0.00027 | 0.00316 ± 0.00021 | 0.00361 ± 0.00033 | 1 |
| 35 | 2364.92923 ± 0.00118 | 0.00192 ± 0.00034 | 0.00808 ± 0.00187 | 1 |
| 45 | 2378.25545 ± 0.00075 | 0.00185 ± 0.00019 | 0.00523 ± 0.00072 | 1 |
| 46 | 2379.60347 ± 0.00042 | 0.00252 ± 0.00019 | 0.00468 ± 0.00045 | 1 |
| 47 | 2380.95384 ± 0.00035 | 0.00299 ± 0.00019 | 0.00484 ± 0.00038 | 1 |
| 48 | 2382.30534 ± 0.03138 | 0.00262 ± 0.00029 | 0.00429 ± 0.00066 | 1 |
| 49 | 2383.65482 ± 0.00065 | 0.00180 ± 0.00032 | 0.00405 ± 0.00078 | 1 |
| 9 | 2330.13165 ± 0.00169 | 0.00152 ± 0.00028 | 0.01160 ± 0.00234 | 2 |
| 10 | 2331.48471 ± 0.00084 | 0.00174 ± 0.00021 | 0.00739 ± 0.00137 | 2 |
| 11 | 2332.83334 ± 0.02299 | 0.00095 ± 0.00045 | 0.00607 ± 0.00289 | 2 |
| 12 | 2334.18152 ± 0.00097 | 0.00092 ± 0.00046 | 0.00243 ± 0.00152 | 2 |
| 21 | 2346.16120 ± 0.00175 | 0.00095 ± 0.00041 | 0.00494 ± 0.00154 | 2 |
| 22 | 2347.50724 ± 0.00076 | 0.00198 ± 0.00027 | 0.00682 ± 0.00096 | 2 |
| 23 | 2348.85870 ± 0.00098 | 0.00318 ± 0.00089 | 0.00958 ± 0.00205 | 2 |
| 24 | 2350.20992 ± 0.00094 | 0.00200 ± 0.00021 | 0.00695 ± 0.00105 | 2 |
| 25 | 2351.55931 ± 0.00055 | 0.00137 ± 0.00026 | 0.00261 ± 0.00073 | 2 |
| 35 | 2364.88900 ± 0.00115 | 0.00187 ± 0.00035 | 0.00577 ± 0.00195 | 2 |
| 36 | 2366.23833 ± 0.00067 | 0.00184 ± 0.00021 | 0.00459 ± 0.00069 | 2 |
| 37 | 2367.58754 ± 0.00086 | 0.00145 ± 0.00018 | 0.00663 ± 0.00085 | 2 |
| 49 | 2383.61220 ± 0.00081 | 0.00156 ± 0.00031 | 0.00514 ± 0.00129 | 2 |
| 50 | 2384.96188 ± 0.00042 | 0.00249 ± 0.00018 | 0.00534 ± 0.00039 | 2 |
| 51 | 2386.31324 ± 0.00068 | 0.00166 ± 0.00019 | 0.00585 ± 0.00067 | 2 |
| 52 | 2387.66170 ± 0.00065 | 0.00144 ± 0.00022 | 0.00356 ± 0.00075 | 2 |
| 10 | 2331.46583 ± 0.00055 | 0.00208 ± 0.00022 | 0.00413 ± 0.00059 | 3 |
| 11 | 2332.81711 ± 0.00039 | 0.00258 ± 0.00038 | 0.00304 ± 0.00040 | 3 |
| 12 | 2334.16835 ± 0.00039 | 0.00244 ± 0.00023 | 0.00380 ± 0.00040 | 3 |
| 13 | 2335.52029 ± 0.00088 | 0.00127 ± 0.00028 | 0.00332 ± 0.00084 | 3 |
| 23 | 2348.84053 ± 0.00135 | 0.00138 ± 0.00036 | 0.00499 ± 0.00162 | 3 |
| 24 | 2350.19119 ± 0.00100 | 0.00160 ± 0.00022 | 0.00504 ± 0.00123 | 3 |
| 25 | 2351.54429 ± 0.00045 | 0.00193 ± 0.00022 | 0.00368 ± 0.00053 | 3 |
| 26 | 2352.89844 ± 0.00168 | 0.00092 ± 0.00019 | 0.00602 ± 0.00187 | 3 |
| 12 | 2334.15237 ± 0.00053 | 0.00138 ± 0.00026 | 0.00273 ± 0.00055 | 4 |
| 13 | 2335.50433 ± 0.00071 | 0.00113 ± 0.00040 | 0.00199 ± 0.00289 | 4 |
| 21 | 2346.18160 ± 0.00095 | 0.00109 ± 0.00040 | 0.00358 ± 0.00136 | 5 |
| 22 | 2347.53394 ± 0.00141 | 0.00076 ± 0.00041 | 0.00281 ± 0.00397 | 5 |
| 23 | 2348.88640 ± 0.00076 | 0.00166 ± 0.00051 | 0.00346 ± 0.00100 | 5 |
| 35 | 2364.90513 ± 0.00032 | 0.00217 ± 0.00033 | 0.00189 ± 0.00060 | 5 |
| 49 | 2383.63367 ± 0.00098 | 0.00099 ± 0.00036 | 0.00395 ± 0.00168 | 5 |
| 52 | 2387.62708 ± 0.00040 | 0.00180 ± 0.00026 | 0.00254 ± 0.00039 | 6 |
| 53 | 2388.97723 ± 0.00098 | 0.00147 ± 0.00023 | 0.00952 ± 0.00237 | 6 |
| 54 | 2390.33064 ± 0.00092 | 0.00105 ± 0.00023 | 0.00350 ± 0.00091 | 6 |

For quantitative constraints on the obliquity, we adopted the likelihood function

$$L = \exp(-\chi^2/2), \tag{11}$$

where

$$\chi^2 = \sum_{i}^{N_{\rm anom}} \frac{(x_{\rm spot,i} - x_{\rm p,i})^2 + (y_{\rm spot,i} - y_{\rm p,i})^2}{(0.5\,R_{\rm p})^2} + {\rm NDP}. \tag{12}$$

Here, $N_{\rm anom}$ is the number of spot-crossing anomalies, and $x_{\rm spot,i}$, $y_{\rm spot,i}$, $x_{\rm planet,i}$, and $y_{\rm planet,i}$ are the coordinates of the spot and the planet at the time of the $i$th anomaly. With this function, we reward models that place the planet and spot close to each other at the times of the observed anomalies. By choosing a length scale of 0.5 $R_{\rm p}$, we assume that the spot sizes are comparable to the size of the planet or smaller. The NDP term is the nondetection penalty, which adds 100 to $\chi^2$ if there is no observed anomaly at a time when the model predicts one. We acknowledge that the length scale and NDP are chosen *ad hoc*, preventing the quantitative results from being taken too seriously; the purpose of the modeling is simply to demonstrate that low-obliquity solutions are able to account for the most prominent sequences of anomalies.

At first, we identified the three most prominent series of spot-crossing anomalies (labeled with red, blue, and magenta arrows in Figure 1) and analyzed each of these families separately with a one-spot model. Then after being satisfied that they gave consistent results, we performed a joint analysis

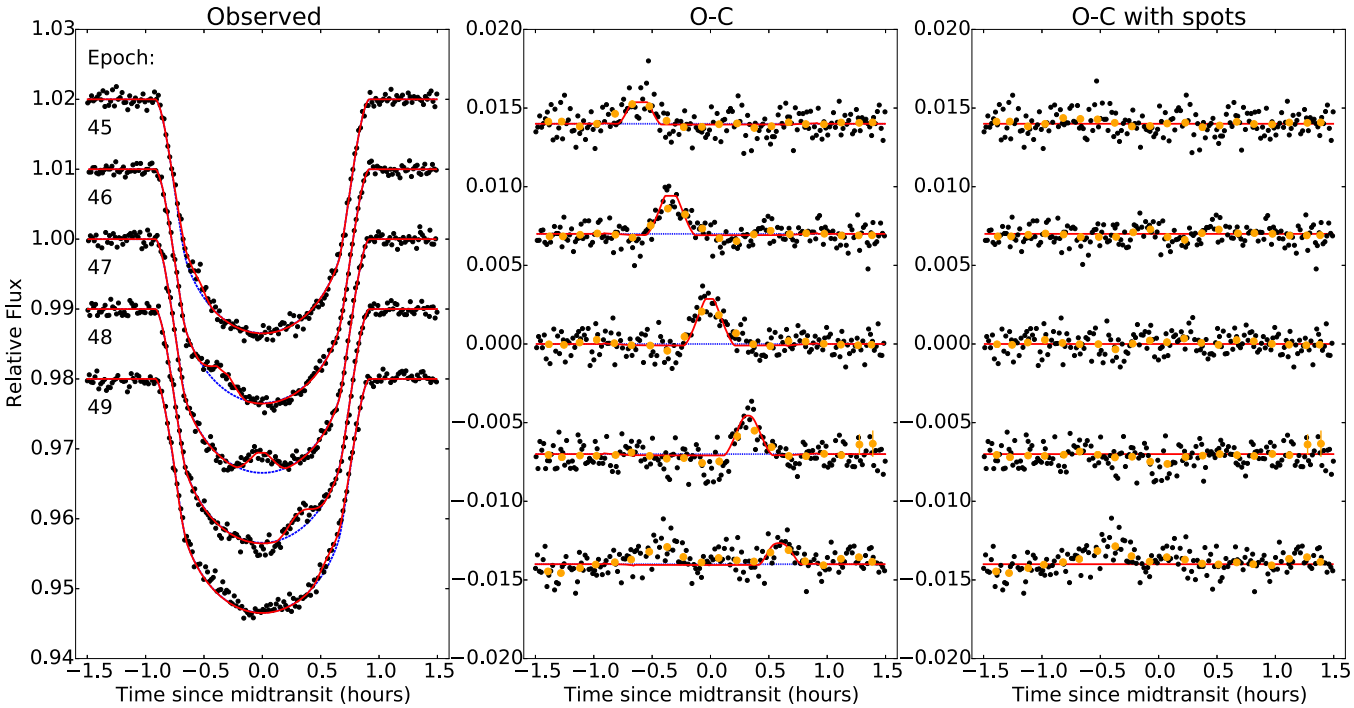


**Figure 7.** Left. The five consecutive transit light curves that were selected for detailed modeling. Arbitrary vertical offsets have been applied to data from different epochs. The dotted blue line is the best-fitting model with no spots. The solid red line is the best-fitting single-spot model. Middle. Residuals after subtraction of the no-spot model. The spot-crossing anomalies are seen to progress steadily in phase from one transit to the next, at the rate that is expected, based on the orbital period and the stellar rotation period. Right. Residuals after subtraction of the single-spot model.

of all the spot-crossing anomalies using a three-spot model. Table 4 gives all the results, based on an MCMC analysis. We reiterate that the quantitative results are contingent on the choice of length scale and NDP in the likelihood function, which were chosen somewhat subjectively. The main point is that in all cases, the sky-projected obliquity is consistent with zero, and the stellar rotation period is consistent with the independently measured period of 18.5 $\pm$ 1.9 days. The stellar inclination $i_\star$ and spot latitude $l$ are only loosely constrained, and their uncertainties are strongly correlated, demonstrating another limitation of this modeling approach.

### 7.2. Light-curve Fitting

As a second approach to demonstrate the low obliquity of Qatar-2, we constructed a numerical model for loss of light due to planetary transit over a star with circular starspots (see Figure 7 for the fitted light curve and Figure 8 for the model). We used a two-dimensional Cartesian grid to represent the stellar disk and assigned intensities to the pixels based on the assumed limb-darkening law and the locations of the starspots and the planet. For simplicity the spots were assumed to be circular and uniform in intensity, with unchanging properties and locations in the rotating frame of the star. Thus, in addition to the usual transit parameters, this model has parameters for the spot's angular size ($\alpha$), intensity contrast ($f$), and latitude ($l$) and the time ($t$) when it crosses the $x$-axis. We also allow each spot to be associated with an independent rotation period, $P_{\rm rot,i}$, to allow for a consistency check (and to allow for a modest degree of differential rotation, although we did not end up finding evidence for this effect).

At any particular time, we located the pixels affected by the spot by taking the dot product between the surface normal associated with the pixel and the position vector of the spot. The intensity of any pixel within the angular radius of a spot center was multiplied by the spot's contrast factor. The pixels within the planet's silhouette were assigned zero intensity. Then the summed intensity of all the pixels was compared to the observed flux, and the usual $\chi^2$ statistic was calculated. We held fixed the transit parameters at the best-fitting values obtained in Section 3.

The pixelated model is conceptually straightforward, but it requires two-dimensional integration, which is computationally expensive. Béky et al. (2014) wrote a semi-analytic code called `Spotrod` to model spot-crossing anomalies, also assuming uniform and circular spots. Their algorithm is more computationally efficient because the integration is reduced to one dimension through the analytic calculation of the points of intersection between the spot and the planet. We analyzed the light curve with our own 2-d model as well as with `Spotrod` to check for consistency.

Although more than half of the transits observed by *K2* showed evidence for spot-crossing anomalies, we chose to model five consecutive anomalies with the highest signal-to-noise ratio. We chose to limit the time interval of the model to $\approx$5 days because we were not modeling spot evolution.

First we found the maximum likelihood model using the Levenberg–Marquardt algorithm as implemented in `lmfit`. We then conducted an MCMC analysis with `emcee`. Table 5 gives the results. The results from our 2-d numerical model and `Spotrod` are very similar. The stellar inclination was found to be within about 10° of edge-on, and the sky-projected obliquity was found to be consistent with zero within about 5°. The stellar rotation period was found to agree well with the value reported previously in Section 5. The angular radius of the spot was around 10°, much larger than those of sunspots.

The numerical light-curve modeling may appear to offer very precise constraints on the obliquity and other system

**Table 4**
Results of the Geometric Model

| Parameter | Spot 1 | Spot 2 | Spot 3 | Combined |
|---|---|---|---|---|
| $\lambda$ (°) | 0.0 ± 4.4 | 0.0 ± 4.4 | 0.0 ± 6.3 | 0.0 ± 2.8 |
| $i_s$ (°) | 90 ± 22 | 90 ± 22 | 90 ± 24 | 90 ± 19 |
| $l$ (°) | 1 ± 18 | 2 ± 19 | 1 ± 21 | 2 ± 16 |
| $P_{\rm rot}$ (days) | 17.89 ± 0.14 | 17.98 ± 0.15 | 17.99 ± 0.50 | 17.94 ± 0.10 |

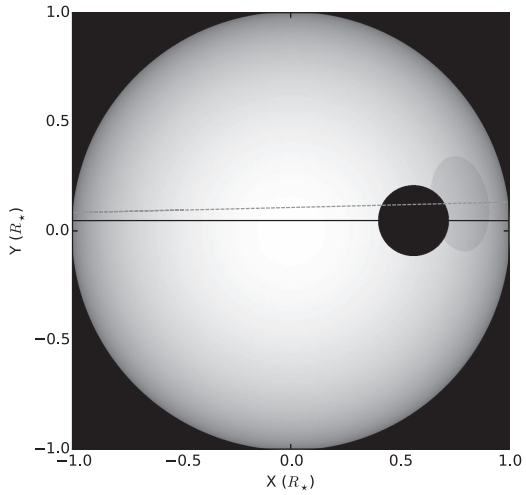


**Figure 8.** Illustration of the best-fitting spot model from Figure 7 at the time of Epoch 49. Visible are the limb-darkened photosphere, the starspot (light gray ellipse near the limb), and the planet (black circle). The dashed line is the spot's trajectory across the stellar disk, and the solid line is the planet's trajectory. A given spot produces smaller anomalies when it is projected near the limb, due to geometrical foreshortening and limb darkening.

**Table 5**
Results of the Numerical Models

| Parameter | Spotrod | Pixelated Model |
|---|---|---|
| $\lambda$ (°) | $1.4^{+3.0}_{-1.7}$ | $4.3^{+4.6}_{-2.7}$ |
| $i_s$ (°) | 89.8 ± 4.0 | 90.1 ± 7.9 |
| $l$ (°) | $6.2^{+7.3}_{-4.2}$ | $5.4^{+7.5}_{-6.8}$ |
| $P_{\rm rot}$ (days) | 18.62 ± 0.31 | 18.54 ± 0.40 |
| $t_{\rm anom}$ (BJD–2454900) | 2380.953 ± 0.025 | 2380.928 ± 0.025 |
| $\alpha$ (°) | 11.2 ± 1.2 | 12.7 ± 0.7 |
| $f$ | 0.90 ± 0.02 | 0.92 ± 0.01 |

parameters. However, just as was the case with our first modeling approach, the precise quantitative results should not be taken too seriously because the light curve models make strong assumptions about the shape and intensity distribution of the spots as well as the lack of any spot migration or evolution. There is no reason to believe that the spots are circular, and indeed, each "spot" may in reality be a complex, splotchy arrangement of spots and plages. We regard the numerical results as a conceptually straightforward demonstration that the obliquity is likely to be smaller than about 10°.

## 8. SUMMARY AND DISCUSSION

In this work, we presented an analysis of the *K2* short-cadence observation of Qatar-2. The continuous monitoring, high precision, and high cadence of the *K2* data helped to refine the transit parameters. In addition, the data quality was high enough to facilitate the identification and exclusion of data points affected by spot-crossing anomalies, leading to a less biased set of transit parameters.

We measured the stellar rotation period of Qatar-2A, 18.5 ± 1.9 days based on the out-of-transit flux variation of the *K2* light curve. Using the technique of gyrochronology, the rotation period led to an independent estimate of the stellar age, 1.4 ± 0.3 Gyr. The rotation period also played a crucial role in our obliquity determination; the lack of an independently measured rotation period had been a missing piece of the puzzle in a previous effort to determine the stellar obliquity.

The nondetection of a secondary eclipse allowed us to place a constraint on the planet's geometric albedo in the *Kepler* bandpass, $A_g < 0.06$, with 95% confidence. This is consistent with previous investigations that showed "hot Jupiters" often have low albedos (Kipping & Spiegel 2011; Gandolfi et al. 2013; Esteves et al. 2015).

We detected ELV and DB effects in the *K2* light curve after filtering out long-term stellar variability and systematic effects. The magnitudes of these two effects imply a planetary mass of 2.6 ± 0.9 $M_{\rm Jup}$ and 3.9 ± 1.5 $M_{\rm Jup}$, both of which are consistent with the mass determined from the spectroscopic Doppler technique (Bryan et al. 2012). We have updated the ephemerides of Qatar-2b with the new midtransit times observed by *K2*. There is no evidence for orbital decay, leading to a lower bound on the stellar tidal quality factor $Q'_\star > 1.5 \times 10^4$ (95% confidence).

We identified dozens of spot-crossing anomalies in the *K2* light curve. These anomalies revealed the presence of active regions on the host star along the planet's transit chord. This suggests that Qatar-2 is magnetically active, as one would expect for a star with a relatively young age, which was determined from gyrochronology. We used the observed spot-crossing anomalies to demonstrate that the obliquity of Qatar-2 is very likely smaller than 10°. We did this in two different ways. First we identified individual spot-crossing anomalies and measured their properties, including their times of occurrence. We then used a simple geometric model for which the parameters were determined by requiring spatial coincidences of the spot and the planet at the times of the observed anomalies. In a separate approach, we fitted a photometric model to a portion of the light curve, based on the premise of a planet transiting a limb-darkened star with a circular starspot.

Neither model can be relied upon for precise quantitative results, because of the strong assumptions that were made, such as of a circular shape of the spots and a lack of spot evolution. Nevertheless, the qualitative results leave little room for doubt that the obliquity is lower than 10°. The low obliquity of Qatar-2 is consistent with a pattern that has been previously noted: hot-Jupiter hosts with photospheres cooler than about 6100–6300 K tend to have low obliquities (Winn et al. 2010).

## REFERENCES

Aigrain, S., Parviainen, H., & Pope, B. J. S. 2016, MNRAS, 459, 2408

Barnes, S. A. 2007, ApJ, 669, 1167
Bate, M. R., Lodato, G., & Pringle, J. E. 2010, MNRAS, 401, 1505
Batygin, K. 2012, Natur, 491, 418
Batygin, K., Bodenheimer, P. H., & Laughlin, G. P. 2015, arXiv:1511.09157
Béky, B., Kipping, D. M., & Holman, M. J. 2014, MNRAS, 442, 3686
Bryan, M. L., Alsubai, K. A., Latham, D. W., et al. 2012, ApJ, 750, 84
Carter, J. A., Rappaport, S., & Fabrycky, D. 2011, ApJ, 728, 139
Chatterjee, S., Ford, E. B., Matsumura, S., & Rasio, F. A. 2008, ApJ, 686, 580
Deming, D., Knutson, H., Kammer, J., et al. 2015, ApJ, 805, 132
Eastman, J., Siverd, R., & Gaudi, B. S. 2010, PASP, 122, 935
Esteves, L. J., De Mooij, E. J. W., & Jayawardhana, R. 2015, ApJ, 804, 150
Fabrycky, D., & Tremaine, S. 2007, ApJ, 669, 1298
Foreman-Mackey, D., Hogg, D. W., Lang, D., & Goodman, J. 2013, PASP, 125, 306
Gandolfi, D., Parviainen, H., Fridlund, M., et al. 2013, A&A, 557, A74
Gaudi, B. S., & Winn, J. N. 2007, ApJ, 655, 550
Howell, S. B., Sobeck, C., Haas, M., et al. 2014, PASP, 126, 398
Kipping, D. M., & Spiegel, D. S. 2011, MNRAS, 417, L88
Kreidberg, L. 2015, PASP, 127, 1161
Levrard, B., Winisdoerffer, C., & Chabrier, G. 2009, ApJL, 692, L9
Lin, D. N. C., Bodenheimer, P., & Richardson, D. C. 1996, Natur, 380, 606
Lomb, N. R. 1976, Ap&SS, 39, 447
Luger, R., Agol, E., Kruse, E., et al. 2016, arXiv:1607.00524
Mancini, L., Southworth, J., Ciceri, S., et al. 2014, MNRAS, 443, 2391
Mancini, L., Southworth, J., Ciceri, S., et al. 2016, MNRAS, 462, 4266
Maxted, P. F. L., Serenelli, A. M., & Southworth, J. 2015, A&A, 577, A90
Mazeh, T., & Faigler, S. 2010, A&A, 521, L59
Močnik, T., Southworth, J., & Hellier, C. 2016, arXiv:1608.07524
Newville, M., Stensitzki, T., Allen, D. B., & Ingargiola, A. 2014, LMFIT: Non-Linear Least-Square Minimization and Curve-Fitting for Pythonű, Zenodo, doi:10.5281/zenodo.11813
Nutzman, P. A., Fabrycky, D. C., & Fortney, J. J. 2011, ApJL, 740, L10
Ohta, Y., Taruya, A., & Suto, Y. 2005, ApJ, 622, 1118
Pope, B. J. S., Parviainen, H., & Aigrain, S. 2016, MNRAS, arXiv:1606.01264
Queloz, D., Mayor, M., Weber, L., et al. 2000, A&A, 354, 99
Sanchis-Ojeda, R., & Winn, J. N. 2011, ApJ, 743, 61
Sanchis-Ojeda, R., Winn, J. N., Holman, M. J., et al. 2011, ApJ, 733, 127
Scargle, J. D. 1982, ApJ, 263, 835
Schlaufman, K. C. 2010, ApJ, 719, 602
Silva, A. V. R. 2003, ApJL, 585, L147
Silva-Valio, A., Lanza, A. F., Alonso, R., & Barge, P. 2010, A&A, 510, A25
Vanderburg, A., & Johnson, J. A. 2014, PASP, 126, 948
Vanderburg, A., Latham, D. W., Buchhave, L. A., et al. 2016, ApJS, 222, 14
Winn, J. N., Fabrycky, D., Albrecht, S., & Johnson, J. A. 2010, ApJL, 718, L145